MDPI

Modulation of Solar Wind Impact on the Earth's Magnetosphere during the Solar Cycle

Francesco Carbone [1,*], Daniele Telloni [2], Emiliya Yordanova [3] and Luca Sorriso-Valvo [3,4]

1 National Research Council—Institute of Atmospheric Pollution Research, C/o, University of Calabria, 87036 Rende, Italy
2 National Institute for Astrophysics—Astrophysical Observatory of Torino, Via Osservatorio 20, 10025 Pino Torinese, Italy; daniele.telloni@inaf.it
3 Ångström Laboratory, Swedish Institute for Space Physics, Lägerhyddsvägen 1, SE-751 21 Uppsala, Sweden; eya@irfu.se (E.Y.); lucasorriso@gmail.com (L.S.-V.)
4 Istituto per la Scienza e Tecnologia dei Plasmi, Consiglio Nazionale delle Ricerche, Via Amendola 112/D, 70126 Bari, Italy
* Correspondence: francesco.carbone@iia.cnr.it

Abstract: The understanding of extreme geomagnetic storms is one of the key issues in space weather. Such phenomena have been receiving increasing attention, especially with the aim of forecasting strong geomagnetic storms generated by high-energy solar events since they can severely perturb the near-Earth space environment. Here, the disturbance storm time index *Dst*, a crucial geomagnetic activity proxy for Sun–Earth interactions, is analyzed as a function of the energy carried by different solar wind streams. To determine the solar cycle activity influence on *Dst*, a 12-year dataset was split into sub-periods of maximum and minimum solar activity. Solar wind energy and geomagnetic activity were closely correlated for both periods of activity. Slow wind streams had negligible effects on Earth regardless of their energy, while high-speed streams may induce severe geomagnetic storming depending on the energy (kinetic or magnetic) carried by the flow. The difference between the two periods may be related to the higher rate of geo-effective events during the maximum activity, where coronal mass ejections represent the most energetic and geo-effective driver. During the minimum period, despite a lower rate of high energetic events, a moderate disturbance in the *Dst* index can be induced.

Keywords: magnetohydrodynamics; solar wind; magnetosphere; heliosphere

1. Introduction

The Sun is the primary source of energy for the solar system. As such, it determines the physical conditions of the heliosphere and near-Earth space, and acts as the main driver of the climate of our planet. A detailed understanding of the coupling between the Sun and Earth is of fundamental importance for space weather research [1,2]. Among several different components of such coupling, one fundamental aspect of space weather phenomena concerns the response of the geomagnetic environment to the physical perturbations caused by solar activity.

Fluctuations in the magnetic field within the solar atmosphere act as complex modulations of plasma conditions in the interplanetary space, affecting the fluxes of solar energetic particles (SEP) and cosmic rays, the UV component of the solar spectrum, abruptly emitting explosive events, such as coronal mass ejections (CMEs), and producing sudden changes in the solar wind (SW) density and velocity associated with high speed streams (HSS) (see [3], and reference therein). Plasma and magnetic fluctuations expelled from the solar atmosphere encounter the Earth's magnetosphere, which protects the atmosphere from direct access of the solar plasma. The impact of such fluctuations is associated with

the origin of geomagnetic storms (GSs), which have important effects on our technological society, and possibly affect climate conditions through complex interactions with the Earth's atmosphere. When a CME or an HSS impacts the Earth system, it destabilizes the magnetosphere, generating a GS [4]. During a GS, the main magnetospheric currents and the connected ionospheric currents are intensified, causing rapid changes in the geomagnetic field. These variations generate geomagnetically induced currents (GICs) that can severely damage the operation of power grids, magnetic surveying, etc. [5]. Moreover, GSs also heat the ionosphere, changing its density and composition and perturbing signals propagating through this region, such as radio and global navigation satellite system communications [6]. These effects can seriously affect our technological society, and deserve to be thoroughly investigated.

The Earth's magnetosphere is continuously connected to the ionosphere. The magnetosphere-ionosphere system represents an active element that exhibits very complex dynamics (see [7], and references therein). The response of this system to changes in the interplanetary medium is non-linear, intermittent, and scale-invariant, showing several features common to open, extended stochastic systems, usually in an out-of-equilibrium configuration, near criticality [8,9], manifested as across-scale coupling processes. These phenomena and processes, which are highly structured in space and time (e.g., wave dissipation, turbulence, electric field fluctuations), can produce effects at large scales. At the same time, large-scale phenomena create local conditions that can either promote or suppress the development of rapidly changing structures at small spatial scales (e.g., instabilities and turbulence). These features are observed during geomagnetic storms and sub-storms, which implies the occurrence of rapid variations in the geomagnetic field, auroral displays in the polar ionosphere [10] and fast intensification of atmosphere-ionosphere-magnetosphere (AIM) current systems [11]. However, despite the efforts of the scientific community [5,12,13], the understanding of the physical phenomena occurring in the circumterrestrial environment in response to geomagnetic storms is far from being complete.

The intensity of a storm can be quantified by the disturbance storm time index, *Dst*, which is a local time average of the depression measured along the magnetic equator. *Dst* is thus conventionally designed to estimate the ring current intensity and, in turn, to monitor the storm severity. Generally, GSs can be classified as moderate, intense, or super storms, according to the value reached by the *Dst* index during the geomagnetic event: $Dst \in (-100, -50]$ nT, $Dst \in (-250, -100]$ nT, and $Dst \in (-\infty, -250]$ nT, respectively [14].

The release of solar wind energy to the near-Earth space environment severely perturbs the magnetosphere-ionosphere current system, causing the geomagnetic disturbances outlined above. During GSs, a large amount of solar wind (kinetic and magnetic) energy is transferred to the Earth's magnetosphere, through magnetic reconnection at the dayside magnetopause, allowing the solar wind to be linked to the magnetosphere. In fact, high kinetic energy may compress the magnetosphere on the sunward side. On the other hand, the solar wind magnetic energy might be converted into thermal energy, heating the ionosphere and the thermosphere and leading to their expansion. Therefore, the energy content of the SW appears to be a crucial variable to study the relationship between the SW driver and the magnetospheric response in the field of space weather research.

Within this framework, this manuscript represents a follow-up paper to previous reports [15,16] devoted to the analysis of the correlation between solar-wind energy and the *Dst* index. Here, we focus on investigation of the solar activity level and its correlation with the *Dst* disturbances during a period spanning 12 years occurring in the interval from January 2005 to December 2016. The analysis was performed using an in situ magnetic field and plasma measurements recorded using a magnetic field investigation fluxgate magnetometer [17] and a solar wind experiment Faraday cup instrument [18] onboard a Wind spacecraft, orbiting around the Lagrangian point L1 upstream of the Earth. The original dataset was split into two separate sub-samples, for periods of maximum (2012–2014) and

minimum (2007–2009) solar activity, to compare the geo-effectiveness response to the solar wind energy in the two different conditions.

2. Methodology

To study the impact of solar activity on *Dst*, three magnetohydrodynamic (MHD) quantities were investigated, i.e., the kinetic energy $E_v = \int \mathbf{V}^2 \, d^3\mathbf{r}$, the magnetic energy $E_b = \int \mathbf{B}^2 \, d^3\mathbf{r}$, and the total energy $E_t \equiv E_v + E_b$, where $\mathbf{B} = \mathbf{b}/\sqrt{4\pi\rho}$ is the magnetic field in Alfvèn (velocity) units, with ρ the solar wind mass density, and $\mathbf{V}$ the solar wind velocity [13,19]. Such quantities were obtained from in situ measurements with resolution $\Delta t = 92$ s [17,18]. The measurements were downsampled to $\Delta t = 3600$ s in the last step of the analysis so that comparison with the *Dst* index could be performed using data with a similar sampling time. Because of the strongly statistical nature of the analysis and the robustness of the wind database, no pre-processing of the data was necessary. In the first three rows of Figure 1 are reported the temporal evolution for the total magnetic field $|B|$, the solar wind bulk velocity V, and the solar wind density ρ for two CME events observed during the period 15 July 2012 06:00:00→17 July 2012 05:00:00 ($Dst = -139$, left panels), and 6 August 2011 22:00:00→7 August 2011 22:00:00 ($Dst = -115$, right panels) [20]. The vertical dashed lines represent the CME duration.
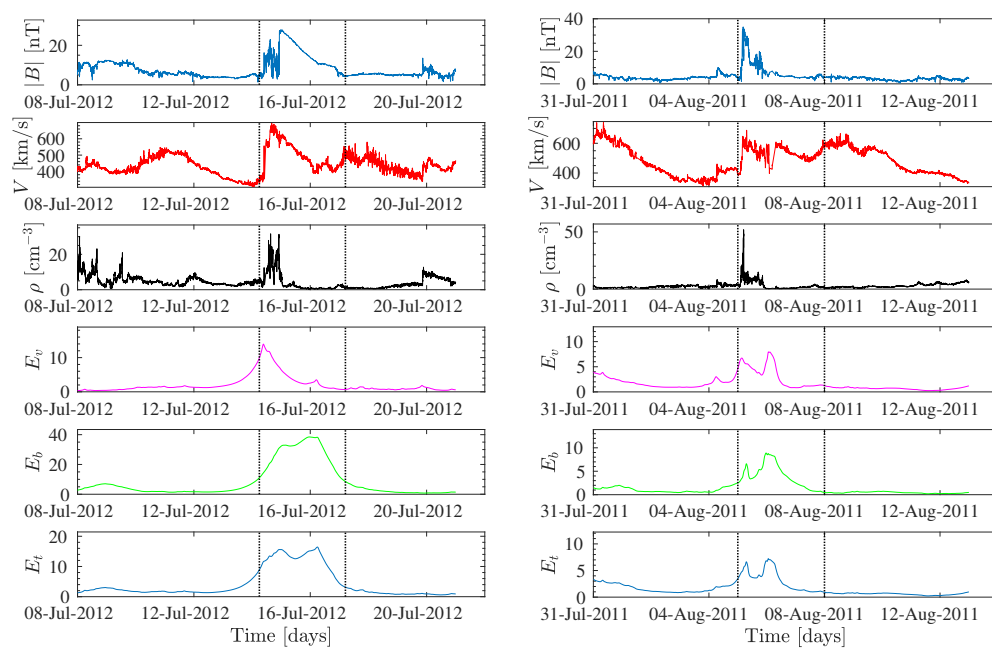

Figure 1. From top to bottom: temporal evolution of the total magnetic field $|B|$, solar wind bulk velocity V, and the solar wind density ρ for two samples measured by Wind spacecraft: left column 15 July 2012 06:00:00→17 July 2012 05:00:00 $Dst = -139$, right column 6 August 2011 22:00:00→7 August 2011 22:00:00 $Dst = -115$. The vertical dashed lines represent the CME duration. In the last three panels, the temporal evolution of the integrated quantities E_v, E_b, and $E_t = E_v + E_b$ is reported.

MHD quantities can be investigated in terms of local contributions in the frequency and time domains, by expanding $\mathbf{V}$ and $\mathbf{B}$ through a wavelet transform (WT). The main advantage of using WT compared to Fourier methods is the ability to extract frequency information from a complex time series using temporal windows of variable size u [21]. WT transforms a signal into a series of coefficients associated to different scales and with discrete energies, offering a powerful method to quantify how energy is spatially and

temporally distributed on multiple scales [15,16,21,22]. In light of this, the integral relations for the kinetic and magnetic energy can be redefined as:

$$E_v(u,t) = \frac{1}{2}\sum_{i=1}^{3}\tilde{V}_i(u,t) \tag{1}$$

$$E_b(u,t) = \frac{1}{2}\sum_{i=1}^{3}\tilde{B}_i(u,t), \tag{2}$$

where $\tilde{V}_i(u,t)$ and $\tilde{B}_i(u,t)$ are the WT of the velocity and magnetic field vector components $V_i \rightarrow i \doteq \{v_x(t),\ v_y(t),\ v_z(t)\}$ and $B_i \rightarrow i \doteq \{b_x(t),\ b_y(t),\ b_z(t)\}$, u and t are the wavelet scale (local time scale) and time defining the domain of the WT, and the sum is extended over the entire field-containing region.

The continuous WT of the MHD variables is defined by the convolution of $V_i(t)$ and $B_i(t)$ with an analyzing wavelet function $\Psi_{u,s}(t)$, based on a scheme where $\Psi_{u,s}(t)$ is scaled and shifted along the analyzed signal $F(t)$ (being $F(t) \equiv E_v(t)$ or $F(t) \equiv E_b(t)$) according to [23]:

$$W(u,s) = \langle F(t), \Psi_{u,s}(t) \rangle = \int_{-\infty}^{\infty} F(t) \cdot \Psi_{u,s}^{\star}(t)dt \tag{3}$$

$$\Psi_{u,s}(t) = \frac{1}{\sqrt{s}}\Psi\left(\frac{t-u}{s}\right), \tag{4}$$

where ($\star$) indicates a complex conjugate, and $\Psi u, s(t)$ is the kernel function stemming from a specific wavelet family $\Psi(t)$, u is the scale parameter (stretching), and s determines the location of the wavelet (shift on the time axis) [21]. The appropriate choice of $\Psi(t)$, characterized by its shape, is important for specific applications. For turbulence analysis, several well-localized mother wavelets, such as Morlet [24–26], or Haar [27], are typically used, while, for phase analysis, Hermitian [28] wavelets can be selected. In this investigation, the Paul-wavelet transform was selected as a mother wavelet ($\Psi_n(t) \in \mathbb{C}$, and $n = 4$ is the order), since they are better resolved in the time domain. This family behaves like a Ricker wavelet at low order with respect to its real part, while it approaches a Morlet wavelet for high orders [21]. Moreover, the peak frequency in the spectral domain just equals the wavelet order n [29].

Turbulence causes kinetic and magnetic energy, mostly contained in the large scales, to cascade via non-linear interactions to smaller scales, where they are eventually dissipated [19,30]. Such processes generate strongly irregular field fluctuations that may mask the fine structure of the temporal evolution of $E(t)$. In light of this, to enhance the contribution of the small- or meso-scale structures that superpose to the SW turbulent background, the total energy spectrum $E_t(u,t) \equiv E_v(u,t) + E_b(u,t)$ was compensated with the background spectrum, defined through the global wavelet spectrum [21] as $E_0(u) = \int E(u,t)dt$, at each scale u. An example of the non-dimensional energies $E_v(t)$ and $E_b(t)$ is reported in the last three panels of Figure 1 for the CME recorded during the period 15 July 2012 06:00:00→17 July 2012 05:00:00 (left panels), and 6 August 2011 22:00:00→7 August 2011 22:00:00 (right panels).

The shape and dynamical properties of the magnetosphere are strongly regulated by the SW through a direct exchange of energy, mass and momentum [31]. Geomagnetic storms are caused by magnetic reconnection between southward directed IMF and the oppositely directed geomagnetic field at the low-latitude magnetopause region of the dayside magnetosphere. The solar wind magnetic flux is then transferred into the magnetosphere, inflating the magnetotail and storing the energy there, until the pressure build-up cannot be maintained and reconnection on the night-side releases the stored energy, transferring and depleting the magnetic flux back to the day-side. Additionally, a finite time is required for the magnetospheric perturbation to propagate to the magnetosphere-ionosphere current system. Therefore, the two datasets should be synchronized, considering the different

specific regions of space where the measurements were collected. Moreover, only a finite subset of wavelet scales $u \in [u_{\min}, u_{\max}]$ will be taken into account, for both maximum and minimum solar activity periods. This range was accurately selected for reconstructing the total dimensionless energy spectrum:

$$E(t) = \int_{u_{\min}}^{u_{\max}} E(u,t)[E_0(u)]^{-1} du. \tag{5}$$

Finally, it should be pointed out that the downsampling of the data was performed for the energy spectrum $E(t)$.

The lower limit of the integral Equation (5) is simply dictated by the resolution of the *Dst* index and was set to $t_{\min} = 1$ h. On the other hand, the upper limit is extrapolated from the cross-correlation (CC) of the two variables ($\mathscr{C}_{E,Dst}$) as a function of the temporal lag ℓ, defined:

$$\mathscr{C}(\ell) = \frac{\sum_{i=1}^{N-\ell}(E_i - \langle E \rangle)(Dst_{i+\ell} - \langle Dst \rangle)}{\sqrt{\sigma_E}\sqrt{\sigma_{Dst}}}, \tag{6}$$

where $\langle E \rangle$, and $\langle Dst \rangle$ are the means of the two populations, σ_E and σ_{Dst} are their associated variances, ℓ is the temporal lag and N the total number of observations. In Figure 2 the CC is shown for various lag times ranging from $\ell = 1$ h to $\ell = 1000$ days, for both the solar minimum (blue symbols) and the solar maximum (red symbols) periods.
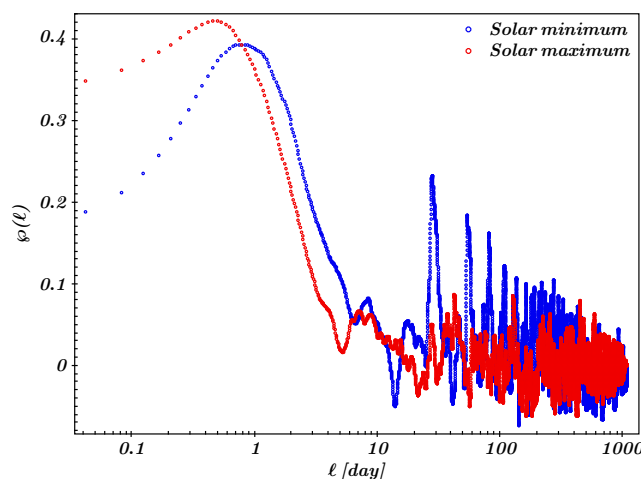

Figure 2. Cross-correlation function for total energy E and Dst index measured for the maximum activity period (red symbols) and minimum activity period (blue symbols) as a function of the lag time ℓ.

The CC peak is observed at a lag time $\ell_{\text{maximum}} \approx 0.4$ days (9 h) for the solar maximum period, and is slightly shifted to a larger scale during the minimum period, $\ell_{\text{minimum}} \approx 0.8$ days (19 h). In both cases, the CC reaches the first zero-crossing for $\ell \approx 10$ days. Moreover, for both cases a broad peak is present, a fingerprint of the fact that the analysis encompasses multiple phenomena that could give rise to variations in the *Dst* index. In fact, such a temporal lag represents the average of the broadly distributed shift times between the two datasets, or, in other words, the time required for the various geo-effective structures to transit from L1 to the Earth. The signature of the 27-day solar rotation is evident in the secondary peaks observed during the minimum period [32,33]. Therefore, to determine the influence of the SW energy on geo-effectiveness, in the following analysis, the energy time series are shifted backward by a time interval ℓ with respect to the *Dst* index: $E(t) = E(t + \ell)$. Finally, the large temporal scale $u_{\max}$, representing the correlation length of the two datasets, is extrapolated from the CC as the time lag at which the peak in $\mathscr{C}$ is reduced to a value e^{-1}, resulting in $u_{\max} = 73$ h for the period of maximum activity

and $u_{\max} = 96$ h for the period of minimum activity. For $u > u_{\max}$ the two datasets are considered to be completely decorrelated.

3. Results and Discussion

An empirical indication of how the geomagnetic activity is affected by the energy content of the SW can be obtained by constructing the two-dimensional bivariate histogram on the *E-Dst* plane. In Figure 3, we show the distributions of the *Dst* index as a function of the total (top panels), kinetic (middle panels), and magnetic (bottom panels) energy, during the intervals of maximum activity (left panels) and of minimum activity (right panels). The black line tracks the maximum of the distributions in each energy bin, giving the most probable values of the *Dst* index within the 68% confidence bounds, indicated as the gray shaded area. A clear link between the enhancement of *Dst* and the total energy carried by the SW is observed for both periods. Indeed, most of the events causing a sensible disturbance ($Dst \leq -10$ nT) correspond to SW energy in the range $E \in [1, 10]$. Nearly zero *Dst*, indicating an unperturbed current system, is observed for $E_t \leq 0.2$ for the maximum activity period, and for $E_t \leq 0.4$ for the minimum activity period. A similar behavior is observed for the distributions $Dst - E_v$ (kinetic energy), and $Dst - E_b$ (magnetic energy), shown respectively in the central and bottom rows of Figure 3. A roughly logarithmic decay is observed for all distributions. In general, faster decay is seen for the maximum activity period. During this period, the decay rate is not constant, but, instead, shows a break and a faster decay when the energy exceeds $E_b, E_t > 2$, or $E_v > 4$. This is the signature of the stronger perturbations in the *Dst* index being associated with larger SW energies. On the other hand, in the period of the solar minimum, a saturation to a nearly constant value, $Dst \approx -20$ nT, is observed at the same $E_t, E_v, E_b \geq 1.8$ for the total, kinetic and magnetic SW energies.

It is evident that, during maximum solar activity periods, severe disturbances, characterized by an index up to $Dst \geq -50$ nT, are observed. Conversely, during the minimum period, the strongest disturbances reach values of the order of $Dst \approx -50$ nT for comparable values of the SW energy. This difference could be related to the different rate of occurrence of events generating GSs. Indeed, during maximum activity the solar wind typically carries more frequent disturbances that impact on the magnetosphere than at the minima of activity. Therefore, the typical recovery time before successive events affecting the *Dst* index is short and does not allow the relaxation of the magnetospheric configuration, so that energy (and therefore perturbations) keep on accumulating in the system. As a result, stronger disturbances may be observed. In other words, extreme perturbations can be linked to the superposition of several events occurring during a short time interval, whose energy accumulates, "charging" the magnetosphere. On the other hand, during the minimum activity period, extreme events are generated at a lower rate, so that geo-effective events are more sparse. After an event, the system has more time for relaxing and reorganizing the local magnetospheric structure, so that the total response does not reach the severity of the maximum activity case.

Finally, to evaluate the role of the SW speed, Figure 4 shows the distributions of the median values of the SW bulk speed V in the *E-Dst* plane. During the solar maximum period (left panels), a large cluster of events located in the core region of the distribution has SW speed $300 \leq V \leq 550$ km s^{-1}, carrying a total energy $E_t \in [0.3, 1]$, with the *Dst* index indicating weak geomagnetic storm activity $Dst \in [-10, -50]$. Such a cluster represents the peak of the distributions seen in Figure 3 within the 68% confidence bounds. On the other hand, the peripheral left and right regions of the distribution are relative to either low- or extreme-energy wind, respectively. A slow wind plasma with speed $250 \leq V \leq 300$ km s^{-1} (corresponding to a stable region with respect to magnetospheric ring currents expected for $Dst = 20$ on quiet days [34]) fills a portion of the plane with energies spanning the range $0.01 \leq E_t \leq 0.3$ and with positive or close to zero *Dst*. This indicates that low-speed flows have a negligible impact on the geomagnetic field, regardless of the kinetic energy levels transported. Stronger geomagnetic activity is observed for high speed streams, where the

Dst index reaches extreme values of the order of $Dst < -100$ nT. In such conditions, the SW average bulk speed lies in the range $V \in [500, 800]$ km s^{-1}, and higher kinetic energy levels $5 < E \leq 10$ are present. This is probably associated with compressive regions generated at the interface between fast and slow flows, where CMEs are more geo-effective drivers. The same trend is also observed for the distribution of the kinetic and magnetic energy (Figure 4 second and third row, left column).

During the minimum activity period (right column), the distribution presents a rather simple shape, stretched along the energy direction in the energy range $E \in [0.02, 10]$ and compressed in a small region of *Dst* values in the range $Dst \in [20, -50]$. All distributions present a neat separation in terms of wind velocity around $Dst \approx 0$, as shown by the fact that the plane is divided into two portions. Positive *Dst* are characterized by low speed streams $V \in [250, 500]$ km s^{-1}. For $Dst < 0$, only higher speed streams are recorded, characterized by a mean bulk speed $V > 500$ km s^{-1}, and the wind is always able to trigger moderate disturbances in the *Dst* index.
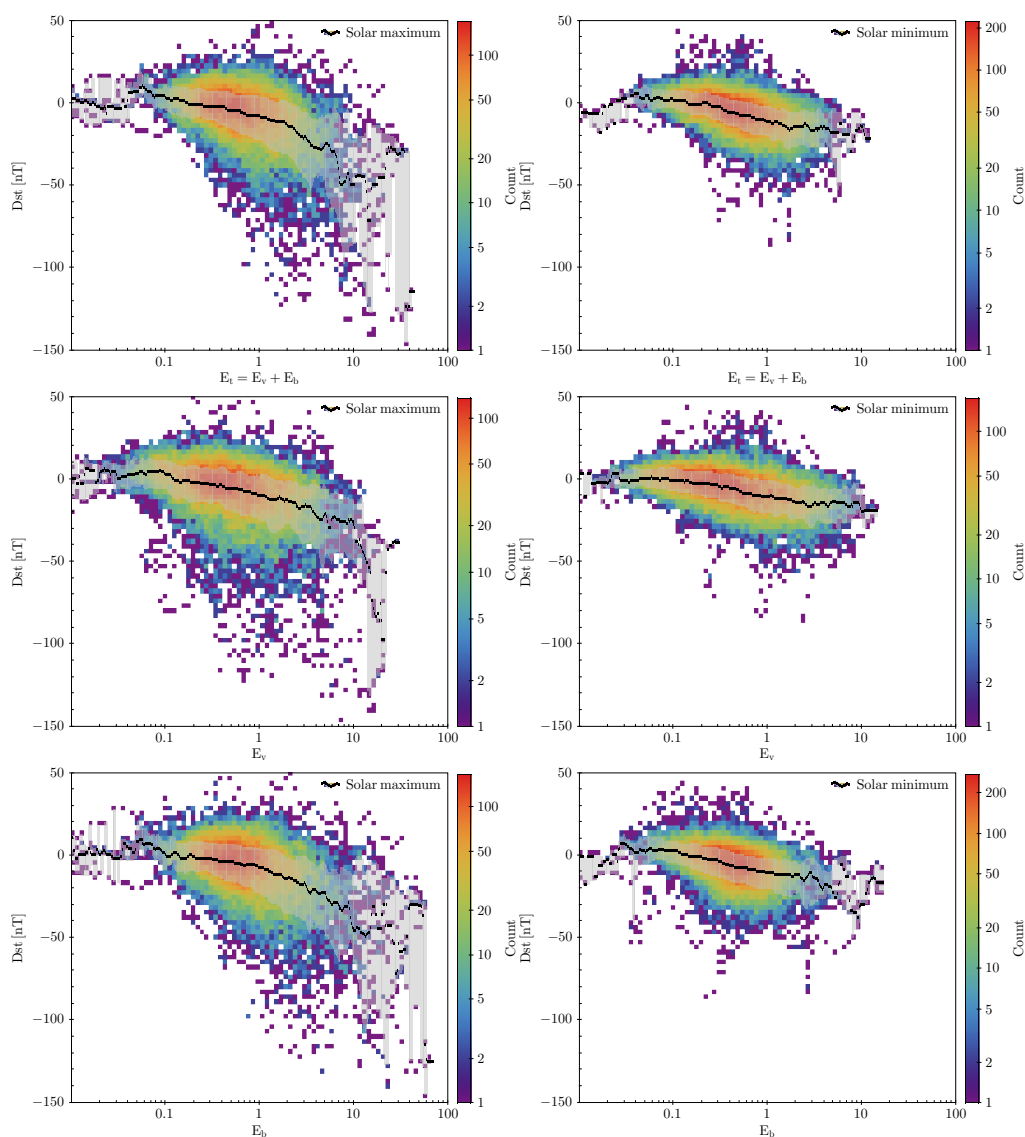

Figure 3. Bivariate histograms of the *Dst* index measurements as a function of the SW energy total energy (**first row**), kinetic energy (**second row**), magnetic energy (**third row**), respectively, for maximum (**left column**) and minimum (**right column**) solar activity periods. The black solid line represents the most probable *Dst* value at each energy level, within the 68% confidence bounds indicated by the shaded gray area.
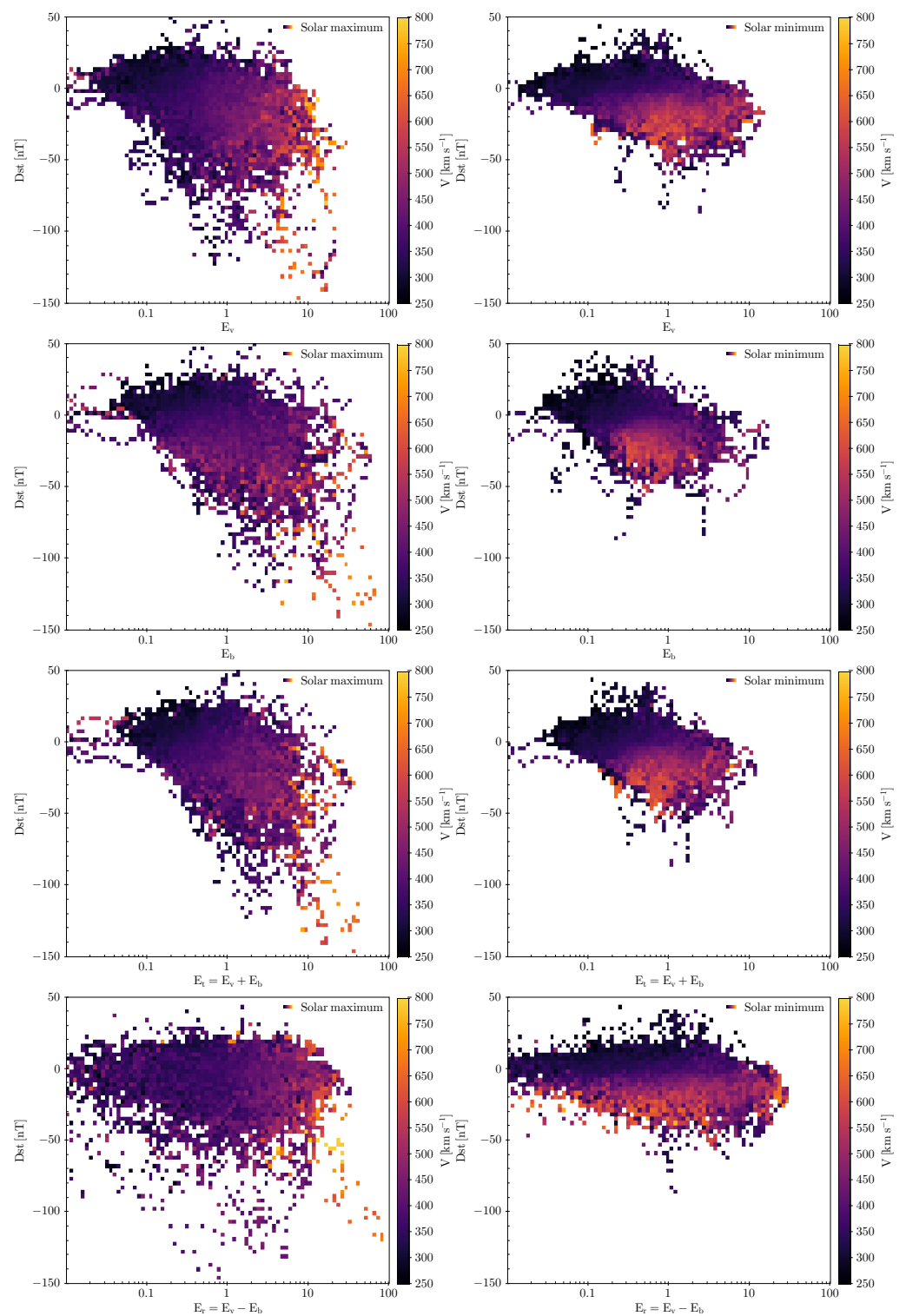
Figure 4. 2D histogram of the median value of the solar wind bulk speed V in the $E - Dst$ plane observed during the maximum (**left panels**) and minimum (**right panels**) activity periods. First row: kinetic energy E_v, second row: magnetic energy E_b, third row: total energy E_t, and fourth row: residual energy $E_r = E_v - E_b$.

The bottom row of Figure 4 shows the bivariate distribution of Dst and residual energy, $E_r = E_v - E_b$. During both maxima and minima, higher values of residual energy are accompanied by stronger perturbations in the Dst indexes (higher geo-effectiveness), showing that E_v is a stronger driver for Dst disturbances. Moreover, the enhanced role

of the solar wind bulk speed during minima is evident; conversely, at maxima, the geo-effectiveness is similar for all wind speeds.

4. Conclusions

In this study, the response of the magnetosphere to different solar wind conditions was investigated statistically by analyzing the correlation between the SW energy and the *Dst* index separately for periods of maximum and minimum solar activity. The results showed a roughly logarithmic decay of *Dst* versus *E*, where higher values of the energy carried by SW correspond to severe storms detected by lower values of the *Dst*.

In addition, the decay observed in the *Dst* as the SW energy increases is different during solar maximum and minimum activity periods. The most severe perturbations, characterized by lower values of *Dst*, occur mostly during solar maxima. However, this does not appear to depend on the SW energy level, as one could expect. We conjecture that this observation could be related to the rate of occurrence of the solar wind perturbations. Perturbations with sufficiently geo-effective energy content are more frequent during solar maxima with respect to solar minima periods. This could lead to the accumulation of perturbations during a shorter time period, which prevents the magnetospheric magnetic configuration from relaxing, therefore leading to severe events with large negative *Dst* indices. On the other hand, during the minimum period, the quiet time between successive events is longer, resulting in moderate *Dst*, due to the slower accumulation of geo-effective events and the subsequent possibility for the magnetospheric currents system to recover the equilibrium configuration. This may be of relevance for space weather research, and, in particular, the determination of the effective duration of perturbations in response to the solar wind drivers.

References

1. Schrijver, C.J.; Kauristie, K.; Aylward, A.D.; Denardini, C.M.; Gibson, S.E.; Glover, A.; Gopalswamy, N.; Grande, M.; Hapgood, M.; Heynderickx, D.; et al. Understanding space weather to shield society: A global road map for 2015? 2025 commissioned by COSPAR and ILWS. *Adv. Space Res.* **2015**, *55*, 2745–2807. [CrossRef]
2. Koskinen, H.E.J.; Baker, D.N.; Balogh, A.; Gombosi, T.; Veronig, A.; von Steiger, R. Achievements and Challenges in the Science of Space Weather. *Space Sci. Rev.* **2017**, *212*, 1137–1157. [CrossRef]
3. Beedle, J.M.H.; Rura, C.E.; Simpson, D.G.; Cohen, H.I.; Moraes Filho, V.P.; Uritsky, V.M. A User's Guide to the Magnetically Connected Space Weather System: A Brief Review. *Front. Astron. Space Sci.* **2022**, *8*, 253. [CrossRef]
4. Gonzalez, W.D.; Joselyn, J.A.; Kamide, Y.; Kroehl, H.W.; Rostoker, G.; Tsurutani, B.T.; Vasyliunas, V.M. What is a geomagnetic storm? *J. Geophys. Res. Space Phys.* **1994**, *99*, 5771–5792. [CrossRef]
5. Pulkkinen, A.; Bernabeu, E.; Thomson, A.; Viljanen, A.; Pirjola, R.; Boteler, D.; Eichner, J.; Cilliers, P.J.; Welling, D.; Savani, N.P.; et al. Geomagnetically induced currents: Science, engineering, and applications readiness. *Space Weather* **2017**, *15*, 828–856. [CrossRef]
6. Basu, S.; Groves, K.; Basu, S.; Sultan, P. Specification and forecasting of scintillations in communication/navigation links: Current status and future plans. *J. Atmos. Sol.-Terr. Phys.* **2002**, *64*, 1745–1754. [CrossRef]

7. Milan, S.E.; Clausen, L.B.N.; Coxon, J.C.; Carter, J.A.; Walach, M.T.; Laundal, K.; Østgaard, N.; Tenfjord, P.; Reistad, J.; Snekvik, K.; et al. Overview of Solar Wind–Magnetosphere–Ionosphere–Atmosphere Coupling and the Generation of Magnetospheric Currents. *Space Sci. Rev.* **2017**, *206*, 547–573. [CrossRef]

8. Consolini, G. Self-organized criticality: A new paradigm for the magnetotail dynamics. *Fractals* **2002**, *10*, 275–283. [CrossRef]

9. Uritsky, V.M.; Klimas, A.J.; Vassiliadis, D.; Chua, D.; Parks, G. Scale-free statistics of spatiotemporal auroral emissions as depicted by POLAR UVI images: Dynamic magnetosphere is an avalanching system. *J. Geophys. Res. Space Phys.* **2002**, *107*, SMP 7–1–SMP 7–11. [CrossRef]

10. Kamide, Y.; Chian, A. (Eds.) *Solar Atmosphere*; Springer: Berlin/Heidelberg, Germany, 2007; pp. 55–93. [CrossRef]

11. Ganushkina, N.Y.; Liemohn, M.W.; Dubyagin, S. Current Systems in the Earth's Magnetosphere. *Rev. Geophys.* **2018**, *56*, 309–332. [CrossRef]

12. Buzulukova, N. (Ed.) *Extreme Events in Geospace*; Elsevier: Amsterdam, The Netherlands, 2018. [CrossRef]

13. Bruno, R.; Carbone, V. The Solar Wind as a Turbulence Laboratory. *Living Rev. Sol. Phys.* **2013**, *10*, 2. [CrossRef]

14. Cander, L.R.; Mihajlovic, S.J. Forecasting ionospheric structure during the great geomagnetic storms. *J. Geophys. Res. Space Phys.* **1998**, *103*, 391–398. [CrossRef]

15. Telloni, D.; Antonucci, E.; Bemporad, A.; Bianchi, T.; Bruno, R.; Fineschi, S.; Magli, E.; Nicolini, G.; Susino, R. Detection of Coronal Mass Ejections at L1 and Forecast of Their Geoeffectiveness. *Astrophys. J.* **2019**, *885*, 120. [CrossRef]

16. Telloni, D.; Carbone, F.; Antonucci, E.; Bruno, R.; Grimani, C.; Villante, U.; Giordano, S.; Mancuso, S.; Zangrilli, L. Study of the Influence of the Solar Wind Energy on the Geomagnetic Activity for Space Weather Science. *Astrophys. J.* **2020**, *896*, 149. [CrossRef]

17. Lepping, R.P.; Acūna, M.H.; Burlaga, L.F.; Farrell, W.M.; Slavin, J.A.; Schatten, K.H.; Mariani, F.; Ness, N.F.; Neubauer, F.M.; Whang, Y.C.; et al. The WIND magnetic field investigation. *Space Sci. Rev.* **1995**, *71*, 207. [CrossRef]

18. Ogilvie, K.W.; Chornay, D.J.; Fritzenreiter, R.J.; Hunsaker, F.; Keller, J.; Lobell, J.; Miller, G.; Scudder, J.D.; Sittler, E.C.; Torbert, R.B.; et al. SWE, a comprehensive plasma instrument for the WIND spacecraft. *Space Sci. Rev.* **1995**, *71*, 55–77. [CrossRef]

19. Bruno, R.; Carbone, V. *Turbulence in the Solar Wind*, 1st ed.; Lecture Notes in Physics 928; Springer International Publishing: New York, NY, USA, 2016.

20. Richardson, I.G.; Cane, H.V. Near-Earth Interplanetary Coronal Mass Ejections During Solar Cycle 23 (1996–2009) Catalog and summary of properties. *Sol. Phys.* **2010**, *264*, 189–237. [CrossRef]

21. Torrence, C.; Compo, G.P. A Practical Guide to Wavelet Analysis. *Bull. Am. Meteorol. Soc.* **1998**, *79*, 61–78. [CrossRef]

22. Kaiser, G.; Hudgins, L.H. *A Friendly Guide to Wavelets*; Springer: Berlin/Heidelberg, Germany, 1994; Volume 300.

23. Mallat, S. *A Wavelet Tour of Signal Processing the Sparse Way*, 3rd ed.; Academic Press: Cambridge, MA, USA, 2008.

24. Watkins, L.R.; Tan, S.M.; Barnes, T.H. Determination of interferometer phase distributions by use of wavelets. *Opt. Lett.* **1999**, *24*, 905–907. [CrossRef]

25. Alexandrova, O.; Carbone, V.; Veltri, P.; Sorriso-Valvo, L. Small-Scale Energy Cascade of the Solar Wind Turbulence. *Astrophys. J.* **2008**, *674*, 1153. [CrossRef]

26. Farge, M. Wavelet Transforms and Their Applications to Turbulence. *Annu. Rev. Fluid Mech.* **1992**, *24*, 395–458. [CrossRef]

27. Mangeney, A. Intermittency in the Solar Wind Turbulence and the Haar Wavelet Transform. In *Sheffield Space Plasma Meeting: Multipoint Measurements versus Theory*; Warmbein, B., Ed.; ESA Special Publication: Paris, France, 2001; Volume 492, p. 53.

28. Szu, H.H.; Hsu, C.C.; Sa, L.D.; Li, W. Hermitian hat wavelet design for singularity detection in the Paraguay river-level data analyses. In *Wavelet Applications IV*; International Society for Optics and Photonics; Szu, H.H., Ed.; SPIE: Bellingham, WA, USA, 1997; Volume 3078, pp. 96–115. [CrossRef]

29. Luan, Y.; Huang, Y.; Zheng, X.; Cheng, J. Seismic Time-Frequency Analysis Based on Entropy-Optimized Paul Wavelet Transform. *IEEE Geosci. Remote Sens. Lett.* **2020**, *17*, 342–346. [CrossRef]

30. Kolmogorov, A.N. The local structure of turbulence in incompressible viscous fluid for very large Reynolds numbers. *Proc. R. Soc.* **1991**, *434*,1890. [CrossRef]

31. Consolini, G.; De Michelis, P.; Tozzi, R. On the Earth's magnetospheric dynamics: Nonequilibrium evolution and the fluctuation theorem. *J. Geophys. Res. Space Phys.* **2008**, *113*, A8. [CrossRef]

32. Castillo, Y.; Pais, M.A.; Fernandes, J.; Ribeiro, P.; Morozova, A.L.; Pinheiro, F.J.G. Relating 27-Day Averages of Solar, Interplanetary Medium Parameters, and Geomagnetic Activity Proxies in Solar Cycle 24. *Sol. Phys.* **2021**, *296*, 115. [CrossRef]

33. Yu, B.; Scott, C.J.; Xue, X.; Yue, X.; Chi, Y.; Dou, X.; Lockwood, M. A Signature of 27 day Solar Rotation in the Concentration of Metallic Ions within the Terrestrial Ionosphere. *Astrophys. J.* **2021**, *916*, 106. [CrossRef]

34. Burton, R.K.; McPherron, R.L.; Russell, C.T. An empirical relationship between interplanetary conditions and Dst. *J. Geophys. Res. (1896–1977)* **1975**, *80*, 4204–4214. [CrossRef]